ChemPhysChem

ChemPhysChem
Chemistry Europe
European Chemical Societies Publishing

RESEARCH ARTICLE

An Implementation of General Polarization-Resolved Two-Dimensional Electronic Spectroscopy

Hoang Long Nguyen[1] | Nelson Kim Soon Ong[1] | Sanjib Jana[1] | Sachin Prasad[1] | Thanh Nhut Do[2] | Stefano Caffarri[3] | Howe-Siang Tan[1]

[1]School of Chemistry, Chemical Engineering and Biotechnology, Nanyang Technological University, Singapore, Singapore | [2]Department of Physics and Astronomy, Faculty of Science, Vrije Universiteit Amsterdam, Amsterdam, Netherlands | [3]Aix Marseille Université, CEA, CNRS, BIAM, LGBP, Marseille, France

Correspondence: Howe-Siang Tan (howesiang@ntu.edu.sg)

Received: 12 December 2025 | **Revised:** 5 March 2026 | **Accepted:** 7 April 2026

Keywords: 2D spectroscopy | energy transfer | photosynthesis | polarization | ultrafast spectroscopy

ABSTRACT

Two-dimensional electronic spectroscopy (2DES) is a powerful tool to study the dynamics of complex molecular systems. Polarization control in 2DES allows enhancement of selective signals, providing information about the transition dipole orientations and rotational motion. In this work, we discuss an implementation of polarization-resolved 2DES (p-2DES) in the pump-probe beam geometry that simultaneously acquires signals under parallel and perpendicular pump-probe polarizations. This approach is general, as these two sets of signals can be combined as desired to obtain 2DES spectra of various polarization schemes, such as magic angle, cross-peak specific, diagonal-peak enhancing, and anisotropy. We demonstrate the approach using (1) phthalocyanine, a molecular system with two orthogonal electronic transitions and (2) the photosynthetic light-harvesting complex II, which exhibits a highly congested spectrum with many concurrent energy transfer processes. We show how the polarization schemes can help resolve hidden spectral and kinetic features. This implementation can help to streamline the use of p-2DES and provide more insights into the structural and dynamical properties of complex systems.

1 | Introduction

Two-dimensional electronic spectroscopy (2DES) is a powerful ultrafast spectroscopic technique for probing electronic structure and dynamics in complex molecular systems [1–4]. The technique measures dynamical and spectral information with high resolution in time and frequency, providing a detailed picture of the interactions between the energy levels of the system under study. One can understand a typical 2DES experiment as an upgrade of a conventional pump-probe transient absorption spectroscopic experiment. In 2DES, a set of two ultrafast optical laser pulses with an interpulse delay of τ is used to "pump" or excite a system. After a "pump-probe" delay of T_w, the system is then probed by a third laser pulse to measure the transient changes in absorbance along a detection frequency axis. Fourier transformation along the time axis τ between the two pump pulses results in the spreading of spectral information along the excitation frequency dimension. By correlating the excitation and detection frequencies, 2DES provides information, with femtosecond timescales, about the interactions of the electronic energy levels with each other as well as the environment [4–9]. The information on the 2D spectra are resolved as diagonal and cross-peaks, where the latter is the unique feature of 2DES that highlights the interactions and connectivity between different energy levels [10].

2DES can be enhanced through controlling the laser pulse polarizations. As 2DES measures the interactions of the laser pulse electric fields with the electronic transitions present in a system, the interaction strength scales directly with the alignment between the molecular transition dipole moment and the electric field polarization. By carefully designing the polarization of the incident pulses, one can enhance or suppress specific signal pathways,

thereby isolating spectral features that might be obscured otherwise [11]. Polarization control in 2DES thus enables interrogation of transition dipole orientations, revealing the orientational relationship between coupled transitions, structural arrangement between molecules, and rotational dynamics. One of the commonly used polarization schemes is the all-parallel configuration, which provides maximum signal intensity on the diagonal and captures all the third-order nonlinear optical response pathways; and the so-called magic angle (MA) configuration, which sets the relative angle between the pump and probe polarization to $\sim 54.7°$ and measures isotropic population dynamics. More sophisticated schemes have also been introduced, such as the double-crossed scheme that isolates coherence pathways [11–13], or the cross-peak specific scheme that offers suppression of diagonal peaks [14, 15]. Anisotropy, which can be obtained by combining signals from the all-parallel and perpendicular polarization schemes, is used to determine the change in molecular and exciton orientation [16, 17]. Such advantages of polarization control have been repeatedly shown in various works using polarization-resolved 2D experiments (either in visible or IR region) to suppress/enhance specific signals [14, 15, 18–27], isolate beating patterns [13, 28], and obtain anisotropy information [25, 29–32].

It is often the case where separate polarization-resolved 2DES (p-2DES) experiments are needed to be performed to obtain the necessary information. For example, to measure anisotropy, one needs to collect both signals at parallel and perpendicular pump-probe polarizations. Another example is in the cross-peak specific schemes, where it is still necessary to obtain the diagonal peak information to quantify the efficiency of signal suppression followed by a thorough signal analysis [14, 15]. Separate measurements of parallel and perpendicular polarized spectra can also be done and postprocessed to suppress signals and reduce spectral congestion [33–36]. However, not only do the multiple data collection attempts cost more time and effort, the experimental condition may also be inconsistent across the experiments due to changes in laser power and spectra. These inconsistencies require another step of normalizing the intensity and time axes of the datasets [33]. Furthermore, in long duration experiments or those involving sensitive samples, sample integrity becomes an issue over multiple measurements.

In this work, we present an implementation of general p-2DES based on the simultaneous acquisition of parallel and perpendicular polarized spectra within a single measurement. Similar implementations have been shown in fluorescence [37] and 2D infra-red (2DIR) spectroscopy [38]. However, to the best of our knowledge, there has not been any report of such implementation in 2DES, nor has there been any systematic demonstration of the full capability of this approach. This approach is general since the collected datasets, being orthogonally polarized, can be combined as desired, to produce 2DES spectra of various polarization schemes that can highlight different spectral components in the sample system. We provide a detailed description of the scaling of signal intensities in different polarization schemes. We focus our presentation on the pump-probe beam geometry, although the same idea can be applied to other types of beam geometries. We apply the approach in various sample systems to demonstrate its versatility in obtaining p-2DES features, which allows for the analysis of 2DES data with a wider perspective and provides more insights into the underlying system properties.

2 | Principles and Methods

2.1 | Polarization Control of 2DES Signals

In 2DES, the signals can be described using the third-order perturbative expansion of the density matrix, arising from three light-matter interactions between the optical laser pulses and the system of interest. The signal strength is thus dependent on the orientations of the transition dipoles and the laser electric field polarizations. An orientational scaling factor F, indicative of the signal strength, is related to the four-point orientational correlation function containing contributions from the orientational components [10]

$$F = \left\langle \left(\hat{E}_1 \cdot \hat{a}_1\right)\left(\hat{E}_2 \cdot \hat{a}_2\right)\left(\hat{E}_3 \cdot \hat{a}_3\right)\left(\hat{E}_4 \cdot \hat{a}_4\right) \right\rangle \tag{1}$$

Here, $\hat{E}_1 \ldots \hat{E}_4$ represent the electric field polarization vectors, and $\hat{a}_1 \ldots \hat{a}_4$ are the molecular transition dipole moments. The hat notation denotes the unit vector of the corresponding quantities. The first two laser fields are the pump pulses, the third comes from the probe pulse, and a fourth pulse is introduced as the local oscillator (LO) for heterodyne detection of the signals. In principle, the laser pulse polarizations can be independently adjusted. In a pump-probe geometry setup, the pump pulses usually have the same polarizations, and the probe acts as the LO, though this LO polarization can be separately controlled by a polarizer placed after the sample [39]. Equation (1) also takes into account the ensemble average of the orientational distribution of the interacted transitions.

Considering only the incoherent signal pathways (pathways with a population state during the pump-probe delay time), the first two interactions excite a transition ($\hat{a}_1 = \hat{a}_2 = \hat{a}$), and the last two interactions detect or measure a transition ($\hat{a}_3 = \hat{a}_4 = \hat{b}$). In general, the excited and detected transitions are not necessarily the same and can have a relative angle θ_{ab} between the transitions. Using $\hat{X}$ and $\hat{Y}$ as the orthogonal directions in the lab frame, an all-parallel polarization scheme can be denoted as $\langle XXXX \rangle$, while a perpendicular scheme as $\langle XXYY \rangle$. Assuming an isotropic distribution of molecules in the sample, the general formula of the orientational scaling factor F can be found in the work by Hochstrasser [16]. The orientational scaling factors for $\langle XXXX \rangle$ and $\langle XXYY \rangle$ are shown in the first two rows of Table 1. They are expressed in terms of the second-order Legendre polynomial of cos θ_{ab} between the excited and detected transitions. As we focus this work on the pump-probe geometry, cross-polarized schemes ($\langle XYYX \rangle$ and $\langle XYXY \rangle$) are not considered, but possible uses of such schemes will be discussed in section 4.

The behaviors of the scaling factors are plotted as a function of θ_{ab} in Figure 1a. It can be seen that $\langle XXXX \rangle$ signal is reduced in intensity with higher relative angle θ_{ab}, while the $\langle XXYY \rangle$ signal behaves in an opposite manner. For the signal pathways with small θ_{ab}, $\langle XXXX \rangle$ always results in higher signal intensities than $\langle XXYY \rangle$. Signal intensity in $\langle XXYY \rangle$ becomes larger when θ_{ab} approaches 90°. The scaling factors in Table 1 do not account for depolarization effects, that is, changes in the transition dipole orientations due to rotational motion during the pump-probe time delay T_w. Depolarization effects can be described by multiplying

TABLE 1 | Orientational scaling factors of 2D signals of various polarization schemes, along with the combination of $\langle XXXX\rangle$ and $\langle XXYY\rangle$ to obtain such schemes. $P_2(\theta_{ab}) = (3\cos^2\theta_{ab} - 1)/2$, where θ_{ab} is the relative angle between the excited and detected transition. These factors do not account for depolarization effects due to rotation diffusion.

Polarization scheme	Scaling factor
All-parallel $\langle XXXX\rangle$	$\frac{4P_2(\theta_{ab})+5}{45}$
Perpendicular $\langle XXYY\rangle$	$\frac{5-2P_2(\theta_{ab})}{45}$
MA (magic angle) $\frac{1}{3}\langle XXXX\rangle + \frac{2}{3}\langle XXYY\rangle$	$\frac{1}{9}$
CP (cross-peak specific) $-\frac{1}{3}\langle XXXX\rangle + \langle XXYY\rangle$	$\frac{\sin^2\theta_{ab}}{9}$
DP (diagonal-peak enhancing) $\frac{2}{3}\langle XXXX\rangle - \frac{1}{3}\langle XXYY\rangle$	$\frac{\cos^2\theta_{ab}}{9}$
Anisotropy $\frac{\langle XXXX\rangle - \langle XXYY\rangle}{\langle XXXX\rangle + 2\langle XXYY\rangle}$	$0.4P_2(\theta_{ab})$

$P_2(\theta_{ab})$ with an exponential decaying term $D(T_w)$. This turns the scaling factor for the $\langle XXXX\rangle$ scheme, for example, into $\frac{4P_2(\theta_{ab})D(T_w)+5}{45}$. The effect of depolarization converges the scaling factors of $\langle XXXX\rangle$ and $\langle XXYY\rangle$ to the same value, since the excited transition dipoles become isotropic and can be seen in the dashed curves in Figure 1a (see the figure caption for the detailed parameters).

Because signal intensities in parallel and perpendicular polarization schemes depend differently on θ_{ab}, $\langle XXXX\rangle$ and $\langle XXYY\rangle$ can be linearly combined in several polarization schemes to enhance or suppress certain 2DES spectral features

$$F = A\langle XXXX\rangle + B\langle XXYY\rangle \tag{2}$$

For example, polarization schemes to obtain isotropic signals independent of θ_{ab} can be obtained with the linear combination $F_{MA} = \frac{1}{3}\langle XXXX\rangle + \frac{2}{3}\langle XXYY\rangle$ (third row of Table 1). Typically this is achieved in the MA specific experiment where a relative polarization angle of $\emptyset \approx 54.7°$ is set up between the pump and probe pulses, to obtain $\langle XXMM\rangle = \cos^2\emptyset\langle XXXX\rangle + \sin^2\emptyset\langle XXYY\rangle$. Another example combination is the cross-peak specific scheme, termed CP, where the diagonal signals are effectively suppressed by the combination $F_{CP} = 3\langle XXYY\rangle$ - $\langle XXXX\rangle$ [11, 14, 15, 22]. The fourth row of Table 1 provides the scaling factor for this scheme. In this case, the diagonal peaks, which necessarily have excitation and detection on the same transition, will have $\theta_{ab} = 0^\circ$, thus minimizing F_{CP}. In contrast, cross-peaks produced by nonparallel transition dipoles remain and are the strongest when $\theta_{ab} = 90^\circ$.

In general, one can suppress a signal pathway with any relative transition dipole angle θ_s, by combining $\langle XXXX\rangle$ and $\langle XXYY\rangle$ in Equation (2) using coefficients $A = [5 - 2P_2(\theta_s)]$ and $B = -[4P_2(\theta_s) + 5]$. Considering the normalization to better compare with the entries in Table 1, the resulting scaling factor as a function of θ_{ab} is then described by

$$F_{\theta_s}(\theta_{ab}) = \frac{[5 - 2P_2(\theta_s)]\langle XXXX\rangle - [4P_2(\theta_s) + 5]\langle XXYY\rangle}{9\mathrm{sgn}(\theta_s - 45°)} \tag{3}$$

$$= \frac{\cos^2\theta_{ab} - \cos^2\theta_s}{9\mathrm{sgn}(\theta_s - 45°)} \tag{4}$$

As can be seen, F_{θ_s} equals 0 when $\theta_{ab} = \theta_s$, hence suppressing the signal pathways with relative transition dipole angle θ_s. In addition, F_{θ_s} varies monotonically with θ_{ab} and extremizes at $\theta_{ab} = 0^\circ$ and 90°. The spread between the extrema of F_{θ_s} is 1/9, equal to the scaling factor in MA polarization. We apply a sign function $\mathrm{sgn}(\theta_s - 45°)$, taking value of 1 for $45^\circ \le \theta_s < 90°$ and -1 for $0^\circ \le \theta_s < 45°$, to make F_{θ_s} positive for most values of θ_{ab}. A similar expression was reported by Xu et al. [36] to derive the polarization-associated spectra for arbitrary transition dipole relative angles, which was applied in pump-probe spectroscopy to separate the spectral features of a donor–acceptor dyad.

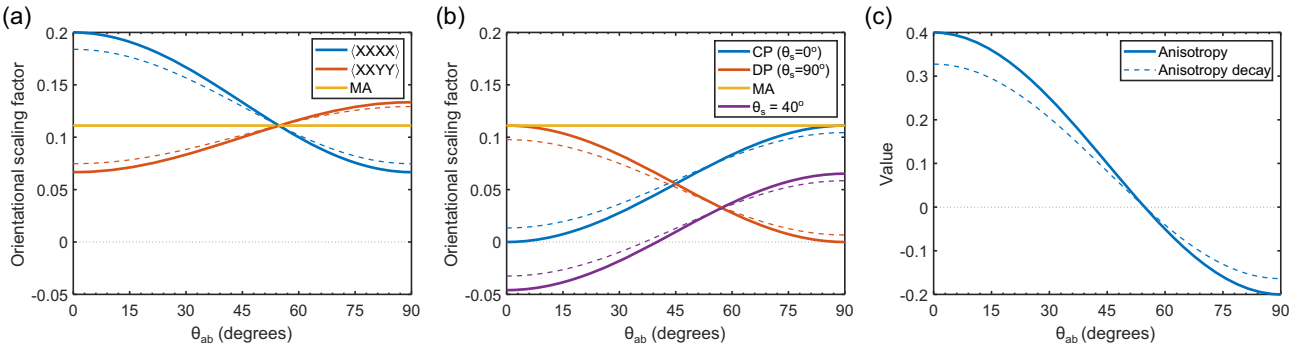

FIGURE 1 | (a) Orientational scaling factors of 2D signal intensities in the all-parallel $\langle XXXX\rangle$ (blue), perpendicular $\langle XXYY\rangle$ (red), and MA (yellow) pump-probe polarization schemes, plotted as a function of the relative angle θ_{ab} between the excited and detected transitions. (b) Similar to (a) but comparing between the CP (blue), DP (red), MA (yellow) schemes, and the scheme that suppresses signals at $\theta_{ab} = 40°$ (purple). (c) The variation of anisotropy with θ_{ab}. In all panels, the dashed curves illustrate the time evolution of the scaling factors by the depolarization term $D(T_w) = \exp(-T_w/\tau_D)$. We use a depolarization timescale of $\tau_D = 500$ ps and simulate the scaling factors at $T_w = 100$ ps.

A few example applications of this formula are given in Table 1 and visualized in Figure 1b. As discussed earlier, in the CP scheme, we can suppress the diagonal peaks by using $\theta_s = 0°$ and hence highlighting the cross-peak signals. In contrast, we can suppress the orthogonal cross-peaks ($\theta_s = 90^\circ$), thus enhancing the diagonal peaks (DP scheme, fifth row in Table 1).

The formula in Equation (3) neglects any depolarization dynamics. We can also take the depolarization dynamics into account by including the depolarization term $D(T_w)$ into $\langle XXXX \rangle$ and $\langle XXYY \rangle$. Equation (3) becomes

$$F_{\theta_s}(\theta_{ab}, T_w) = \frac{2P_2(\theta_{ab})D(T_w) - 2P_2(\theta_s)}{27\mathrm{sgn}(\theta_s - 45°)} \tag{5}$$

This leads to the suppression effect being degraded. The dashed curves in Figure 1b illustrate the degradation compared to the nondepolarized case (solid curves).

The suppression of signals with θ_s other than 0° and 90° is also possible. The signal intensity scales similar to, for example, the purple curve in Figure 1b with $\theta_s = 40°$. In this case, the disadvantage is that signals of the same type can have opposite signs around θ_s. Furthermore, the gradient of the curve around θ_s is large, which makes the suppression less effective because slight deviations of θ_{ab} from θ_s easily cause the signals to appear again. This is opposite to the cases of the CP and DP schemes, where the suppression is more robust as variations of the curves around 0° and 90° are less steep (Figure 1b).

Finally, anisotropy can be calculated to isolate the orientational information, shown in the last row of Table 1. Anisotropy can be used as a direct measurement of the relative orientation between two transitions as well as the depolarization kinetics. Anisotropy is unlike the other polarization schemes mentioned above. Instead, it needs to be derived from two independent schemes such as $\langle XXXX \rangle$ and $\langle XXYY \rangle$. The dependence of anisotropy value with θ_{ab} is illustrated in Figure 1c, which extremizes at 0.4 when $\theta_{ab} = 0°$ and -0.2 when $\theta_{ab} = 90°$. In addition, as is well known, anisotropy can be used to track depolarization dynamics as its value with T_w is directly proportional to the depolarization term, $r(T_w) = 0.4P_2(\theta_{ab})D(T_w)$.

2.2 | Experimental p-2DES Setup

We now describe our p-2DES setup using the pump-probe beam geometry. Laser pulses from a Ti:Sapphire amplifier (Legend, Coherent), centered at 800 nm, 1-kHz repetition rate, are compressed to 50 fs and focused to a home-built pressurized argon gas tube at 2.7 bar absolute pressure. A wedged window is used to split the white light continuum from the argon tube, in which most of the power is transmitted and used as the pump, while the reflected portion is used as the probe. For the pump beam, a single-prism compressor is used for chirp compensation. The pump beam is fed to a pulse shaper (Fastlite, Dazzler), which shapes the input pump pulse into two with programmable delay and phase difference. The pump beam polarization is cleaned by a wire-grid polarizer and set parallel to the optical table. The probe beam is compressed by a pair of chirped mirrors (DCM9, Laser Quantum) and has its pathlength controlled by a translational delay stage (Physik Instrumente). A half-wave plate is used to rotate the probe beam polarization to an angle Ø with respect to the pump beam (in practice, Ø is usually set to near 45°, but the exact angle is not important, as the eventual $\langle XXXX \rangle$ and $\langle XXYY \rangle$ signals are automatically balanced—see Appendix). A beam splitter is used to create a reference beam from the probe. A polarizer is also placed afterwards to clean the probe polarization. The pump, probe, and reference are then focused on the sample space using an off-axis parabolic mirror. At the focal point, the polarization contrast of the pump is 500:1, and the probe is 50:1.

After the sample, a polarizing beamsplitting cube (PBC) splits the probe beam into two polarized components: one parallel (probe 1) and one perpendicular (probe 2) to the pump beam polarization. Another wire-grid polarizer is used to clean the reflected path. The probe 1, probe 2, and reference beams are dispersed and recorded by a charge-coupled device (CCD) array (PIXIS, Princeton Instrument). The CCD array is divided into three horizontal zones, each used to collect one type of signal. The CCD trigger is provided by the laser, and the frame rate is set to 1 kHz.

The transmitted probe beam through the PBC is polarized along $\hat{X}$, and the signal can be represented as

$$\begin{aligned}\langle XX(X\cos Ø + Y\sin Ø)X\rangle &= \cos Ø\langle XXXX\rangle + \sin Ø\langle XXYX\rangle \\ &= \cos Ø\langle XXXX\rangle\end{aligned} \tag{6}$$

where the term $\langle XXYX \rangle$ is essentially zero upon averaging in an isotropic ensemble [10]. The detected signal from the transmitted part through the PBC is equivalent to the $\langle XXXX \rangle$ polarization scheme. A similar argument can be applied to the reflected part, which results in the $\langle XXYY \rangle$ signal. Therefore, the recorded spectra contain two 2D datasets: $S_{\parallel}(\lambda_\tau, T_w, \lambda_t)$ and $S_{\perp}(\lambda_\tau, T_w, \lambda_t)$ respectively the parallel and perpendicular p-2DES signals. λ_τ and λ_t represent the excitation and detection wavelength axes, respectively, and T_w is the time delay of the probe from the second pump pulse. These 2D spectra are considered as the basis spectra for construction of other polarization schemes, as described above.

Figure 2 illustrates the essential schematic of our p-2DES setup. In addition, the sample is contained in quartz cuvettes (Starna) which are found to have minimal birefringent effect to the pump and probe beams. This can be checked by confirming that the probe spectra on the CCD are unchanged while rotating the sample cuvette.

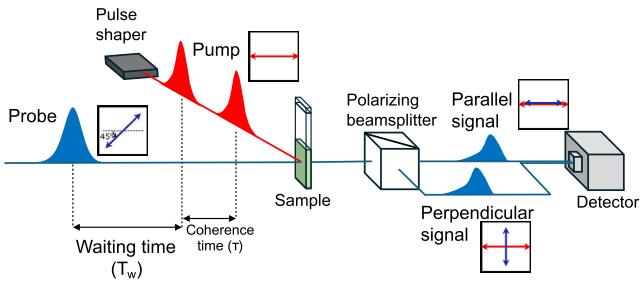

FIGURE 2 | Schematic of p-2DES setup collecting signals at $\langle XXXX \rangle$ and $\langle XXYY \rangle$ polarization schemes simultaneously.

The above-described p-2DES approach has a benefit for concurrent data collection of two orthogonally polarized 2D signals. This ensures that the measurements are performed on the same sample, with identical beam properties such as excitation power and spectra, which results in a reliable consistency between the two collected datasets. Furthermore, the collected polarized signals in our p-2DES setup are automatically balanced. This means that the measured transient absorptions of the two orthogonally polarized 2D signals can be used in the linear combination without any further scaling or normalization (see Appendix).

3 | Applications to Model Systems

3.1 | Spectral Contributions of the Phthalocyanine Q Bands

In this section, we show several experimental demonstrations that utilize the presented implementation of p-2DES to obtain a wide range of polarization-dependent information. Metal-free phthalocyanine (H_2Pc) is a member of the phthalocyanine family, characterized by a planar macrocyclic ring composed of four isoindole subunits (Figure 3a). These isoindoles are interconnected via nitrogen bridges, forming a delocalized π-conjugated system. Compared to porphyrins, which possess only four nitrogen atoms in the macrocycle, phthalocyanines exhibit stronger low-energy Q bands due to the presence of eight nitrogen atoms that helps stabilize the HOMO electron density. Owing to the D_{2h} symmetry of the molecule, H_2Pc features two non-degenerate Q bands, Q_x and Q_y, whose transition dipole moments are perpendicular to each other [40].

The linear absorption spectrum of H_2Pc in 1-chloronaphthalene is presented in Figure 3a. All chemicals were purchased from Sigma-Aldrich. The Q_x and Q_y absorption peaks center at 665 and 700 nm, respectively, with their vibronic progressions extending to the shorter wavelengths (e.g., 640 and 605 nm). In Figure 3b,c, we show the p-2DES spectra at delay time $T_w = 0.1$ ps taken with $\langle XXXX \rangle$ and $\langle XXYY \rangle$ polarization schemes, respectively. In 2DES, negative features represent ground-state bleach (GSB) and stimulated emission (SE) processes, while positive features represent excited-state absorption (ESA). Signal positions on a 2D spectrum are denoted by their excitation/detection (λ_τ/λ_t) wavelengths. The 2D spectra of H_2Pc are dominated by four main negative features: two diagonal peaks at 665/665 (termed S_{xx}) and 700/700 nm (S_{yy}) corresponding to each of the Q bands; two main cross-peaks at 665/700 (S_{yx}) and 700/665 nm (S_{xy}); and several minor cross-peaks connecting to the vibronic progressions.

The scaling differences between the polarization schemes can be clearly observed. In the $\langle XXXX \rangle$ spectrum (Figure 3b), the diagonal peaks are much stronger than the cross-peaks, while the $\langle XXYY \rangle$ spectrum (Figure 3c) appears less contrasted. This is because the Q_x and Q_y transitions are perpendicular to each other, so $\langle XXXX \rangle$ emphasizes the diagonal signals, while the cross-peaks are more enhanced in $\langle XXYY \rangle$.

As shown in the previous section, the diagonal and cross-peaks can be isolated with proper combinations of the $\langle XXXX \rangle$ and $\langle XXYY \rangle$ spectra. We show in Figure 3d and e the 2DES spectra obtained using the CP and DP schemes, respectively. In the CP 2D spectrum, only the S_{yx} and S_{xy} cross-peaks remain. The signal intensity at S_{yy} position is suppressed by > 50 times compared to the isotropic intensity (not shown). Interestingly, small cross-peaks at 640/700

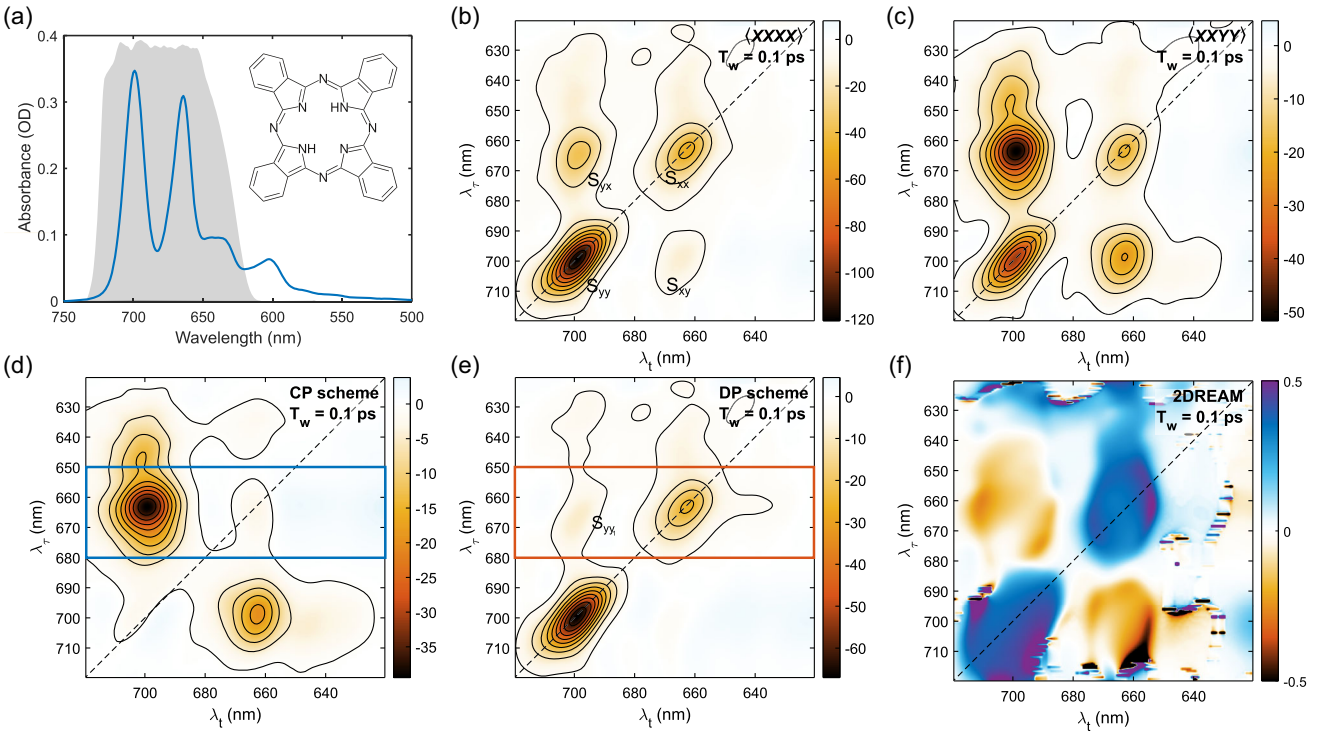

FIGURE 3 | p-2DES spectra of H_2Pc in 1-chloronaphthalene. (a) Linear absorption and the molecular structure of H_2Pc. The shaded area shows the pump spectrum in the 2DES experiment. (b–e) The 2D spectra at $T_w = 0.1$ ps in various polarization schemes, respectively $\langle XXXX \rangle$, $\langle XXYY \rangle$, CP, and DP. Highlighted regions in panels d and e are later subjected to global lifetime analysis. (f) The 2D anisotropy map (2DREAM) at $T_w = 0.1$ ps.

and 700/640 nm persist in the CP 2D spectrum, indicating the coupling between the Q_y electronic transition and the vibronic progression of Q_x. Conversely, in the DP 2D spectrum (Figure 3e), the cross-peaks between Q_x and Q_y are largely suppressed, leaving only the diagonal peaks. However, a small cross-peak at 665/700 nm can still be seen in this spectrum, which likely originates from the vibronic progression of Q_y [40], which would share the same transition dipole moment orientation. This cross-peak is termed S_{yy1}. The shape of S_{yy1} is elongated parallel to the diagonal line, implying a correlation in the energy fluctuations dynamics with the Q_y vibronic progression. The presence of S_{yy1} would be overwhelmed and nonobservable without proper suppression since its amplitude is six times smaller than S_{yx}. This demonstrates the advantage of p-2DES to reveal hidden spectral features.

Figure 3f shows a 2D relaxation of electronic anisotropy map (2DREAM) at T_w = 0.1 ps, illustrating the anisotropy value between every pair of excitation-detection wavelengths. We note that the depolarization process due to rotational diffusion has not occurred at this time delay, therefore, the anisotropy values can reflect directly with the angular difference between the excited and detected states. An averaged anisotropy is obtained at regions where multiple signals overlap. The anisotropy at the diagonal peak S_{yy} is close to 0.4, while at S_{xx} it is 0.33. The cross-peaks have anisotropies of −0.12 for S_{yx} and −0.24 for S_{xy}. Ideally the anisotropy of signals excited and detected from two orthogonal orientations ($\theta_{ab} = 90°$) should be −0.2. The anisotropy of S_{yx} is less extreme due to interference with the vibronic feature S_{yy1}. For S_{xy}, the reason for the anisotropy exceeding the theoretical limit might be due to contributions from ESA features [41, 42].

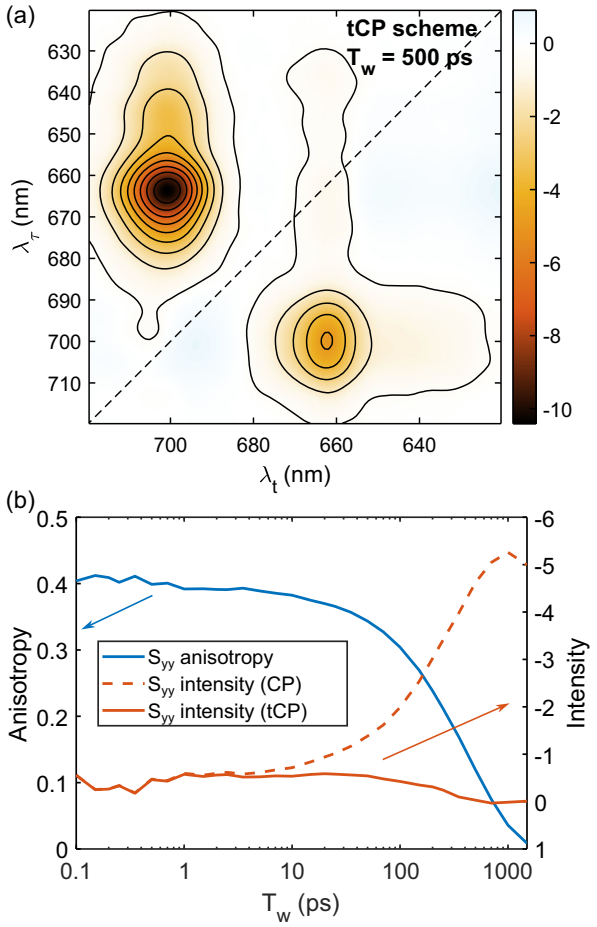

FIGURE 4 | (a) The 2D spectrum at T_w = 500 ps using the tCP schemes, showing that it can suppress diagonal signals at late T_w. (b) The anisotropy decay kinetics (blue) at the S_{yy} diagonal peak, and the intensities of the same peak under CP (dashed red) and tCP (solid red) scheme.

3.2 | Signal Suppression during Depolarization

As can be seen from Equation (5), the suppression of certain 2D signals becomes less effective at late T_w due to depolarization processes which modifies the scaling factors [15]. However, by extracting the depolarization term $D(T_w)$ via the anisotropy decay (already available from the measurement), we can use it to compensate for the effect of depolarization and still be able to maintain the desired signal suppression. This can be done by including the orientational decay term $D(T_w)$, once measured, in Equation (3) and result in the T_w-dependent scaling factor

$$F_{\theta_s}^{\text{enhanced}}(\theta_{ab}, T_w) = \frac{[5 - 2P_2(\theta_s)D(T_w)]\langle XXXX\rangle - [4P_2(\theta_s)D(T_w) + 5]\langle XXYY\rangle}{9\text{sgn}(\theta_s - 45°)} = \frac{\cos^2\theta_{ab} - \cos^2\theta_s}{9\text{sgn}(\theta_s - 45°)} D(T_w) \quad (7)$$

which will always ensure the suppression of signal pathways with $\theta_{ab} = \theta_s$ at any T_w. We demonstrate this by removing the diagonal peaks in the CP 2D spectra of H_2Pc at T_w = 500 ps (Figure 4). We call this the time-dependent CP (tCP) polarization scheme. Figure 4a shows that the 2D spectrum is still diagonal-peak free even though at this T_w, molecular orientational relaxation has occurred as we measure an anisotropy decay of 400 ps lifetime. Figure 4b compares the intensity of the S_{yy} diagonal peak using the CP and tCP schemes. It can be seen that the tCP scheme has the diagonal peak intensity remain around zero. This scheme can be useful when one needs to observe the cross-peak dynamics, especially the peakshape evolution, with a consistent suppression of diagonal peaks.

The downside to this method is that the surviving signals will also decay with $D(T_w)$ as can be seen in Equation (8). This can be understood as at the end of the depolarization process, there are no longer any differences between the $\langle XXXX\rangle$ and $\langle XXYY\rangle$ spectra, and the separation of signal pathways becomes impossible. Furthermore, compared to the CP scheme, the noise level in the tCP scheme is also expected to vary with T_w, because the coefficients in Equation (8) are T_w-dependent. Assuming that the noise levels of the $\langle XXXX\rangle$ and $\langle XXYY\rangle$ signals are comparable, the resulting noise in the combined spectrum scales as $\Delta \propto [5 - 2P_2(\theta_s)D(T_w)] + [4P_2(\theta_s)D(T_w) + 5]$. For the tCP condition, $P_2(\theta_s) = 1$, giving $\Delta \propto 2D(T_w) + 10$, indicating that the noise level decreases slightly as the depolarization process proceeds. Nevertheless, the signal amplitude itself decays with $D(T_w)$, as mentioned above, and therefore the signal-to-noise ratio decreases at long waiting times.

3.3 | Polarization-Dependent Global Lifetime Analysis

To better isolate the kinetics of the spectral components, we subject the 2D data of H_2Pc to global lifetime analysis (GLA). GLA provides a powerful tool for interpreting the time-resolved dynamics in 2D spectra, yielding a set of characteristic lifetimes that describe the dominant spectral evolution processes [43]. Each lifetime corresponds to a 2D decay-associated spectrum (DAS), which reveals the spectral features contributing to that timescale. Here, we use GLA with a parallel kinetic scheme [43] and incorporate it to fit together the CP, DP, and MA 2D spectra of H_2Pc. The fit model can be represented as:

$$\begin{bmatrix} S_{\mathrm{CP}}(\lambda, T_{\mathrm{w}}) \\ S_{\mathrm{DP}}(\lambda, T_{\mathrm{w}}) \\ S_{\mathrm{MA}}(\lambda, T_{\mathrm{w}}) \end{bmatrix} = \sum_{i=1}^{N} \begin{bmatrix} D_{\mathrm{CP}i}(\lambda) \\ D_{\mathrm{DP}i}(\lambda) \\ D_{\mathrm{MA}i}(\lambda) \end{bmatrix} \exp(-T_{\mathrm{w}}/\tau_{\mathrm{i}}) \qquad (8)$$

Here, λ represents the wavelength coordinates on the 2D spectra, N is the number of GLA decay components, τ_i is the decay lifetime of the i-th component, and $D_{\mathrm{CP}i/\mathrm{DP}i/\mathrm{MA}i}(\lambda)$ is the corresponding polarization-dependent 2D DAS. The relationship between the polarization-dependent 2D DAS can be inferred from Table 1 as $D_{\mathrm{CP}i}(\lambda) = \sin^2[\theta_{\mathrm{ab}}(\lambda)]D_{\mathrm{MA}i}(\lambda)$ and $D_{\mathrm{DP}i} = \cos^2[\theta_{\mathrm{ab}}(\lambda)]D_{\mathrm{MA}i}(\lambda)$. Therefore, by taking the amplitude ratio between the resulting DAS, such as $D_{\mathrm{CP}i}$ and $D_{\mathrm{MA}i}$, the angle θ_{ab} of the underlying signal at coordinate λ can be obtained. For simplicity, we have ignored the dependence of the orientational scaling factor on T_{w}, so the depolarization dynamics will appear as an additional GLA component.

We focus on the excitation region of Q_x (λ_τ = 650–680 nm), highlighted in Figure 3d and e. In Figure 5a,b, we show the first 2D DAS, resolved at 140-fs lifetime, from the CP and DP 2D spectra, respectively. Since the original 2D signals are mostly negative, a negative/positive amplitudes of the 2D DAS represent a decay/growth in signal intensity. This 140-fs lifetime shows the contrasting difference between the two polarized spectra. Here, the 2D DAS for the CP scheme (Figure 5a) shows a growth of the S_{yx} cross-peak, while in the DP scheme (Figure 5b) it shows the decay of the S_{xx} diagonal signal. The growth/decay of the S_{yx}/S_{xx} pair represents the internal conversion from the Q_x to Q_y potential energy surface in H_2Pc [7]. The 2D DAS for the DP spectra also exhibits a particular 'butterfly' shape at the S_{xx} and S_{yy1} positions, with negative amplitudes elongated along the diagonal line and positive amplitudes on two sides. This feature indicates spectral diffusion processes, in which the initially nonequilibrium excited state energies relax to an equilibrium, causing the 2D peakshape to change from an slanted-elliptical to a more straight-circular shape [44, 45]. Another observation is that the kinetics of S_{yy1} in Figure 5b does not exhibit any growth. The dynamical differences between S_{yx} and S_{yy1} further emphasize their different origins. Finally, the 2D DAS at MA polarization yields a similar amplitude as the CP polarization for S_{yx} (Figure 5c). As the signals in CP polarization scheme scale as $\sin^2\theta_{\mathrm{ab}}$ relative to MA polarization, this confirms the relative transition dipole angle between the Q_x and Q_y transitions in H_2Pc to be 90°. The complementary use of GLA on p-2DES data highlights the ability to quantify orientational information based on distinguishing kinetics between the polarized 2D signals despite their significant spectral overlap.

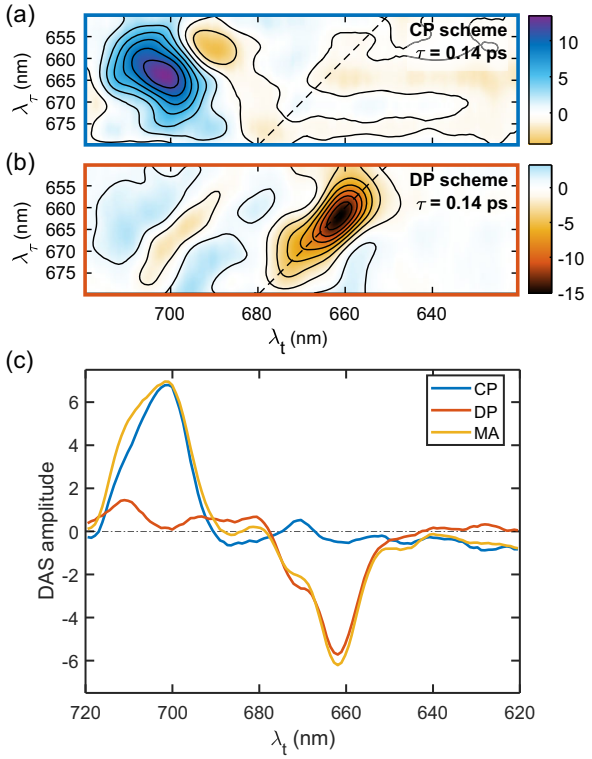

FIGURE 5 | (a,b) The 140-fs 2D DAS component of the CP and DP 2D spectra, respectively, obtained from GLA. (c) Comparison of the λ_τ-integrated amplitudes of the 2D DAS in (a,b), and 2D DAS obtained at the same lifetime for the MA spectra.

3.4 | Elucidating Congested Energy Transfer Steps: A Photosynthetic Light-Harvesting Complex Example

Light-harvesting complex II (LHCII) is the most abundant pigment-protein complex found in the thylakoid membrane of higher plants [46]. LHCII is responsible for the light-harvesting processes as well as photoprotection in plant photosynthesis [47]. Within an LHCII trimer, photoexcitation of a chlorophyll (Chl) molecule can migrate among neighboring Chl sites via excitonic energy transfer (EET) processes. EET in LHCII occurs in a vast network of Chl with timescales ranging from several hundred femtoseconds to a few picoseconds, making LHCII a good representative system for 2DES studies of energy transfer pathways [48].

In Figure 6a, we show the linear absorption spectrum alongside a structural illustration of the LHCII protein surface with the embedded Chl pigments. The LHCII sample was extracted from *Arabidopsis thaliana* as reported previously [49]. The spectrum of LHCII in this wavelength region is congested with signals from 42 Chl *Q*-band transitions [50]. Figure 6b and c present the 2DES spectra of the trimeric LHCII at T_{w} = 0.2 ps, obtained with the MA and CP polarization schemes, respectively. In the MA 2D spectrum (Figure 6b), initial pigment excitations appear as diagonal peaks spanning from 650 to 680 nm. EET processes redistribute excitation from higher- to lower-energy states, resulting in the decays of most diagonal peaks and concurrent growths of cross-peaks [51, 52]. In reality, there are various cross-peaks extending within this region due to heavy spectral congestion. Figure 6c demonstrates how the CP polarization scheme effectively suppresses

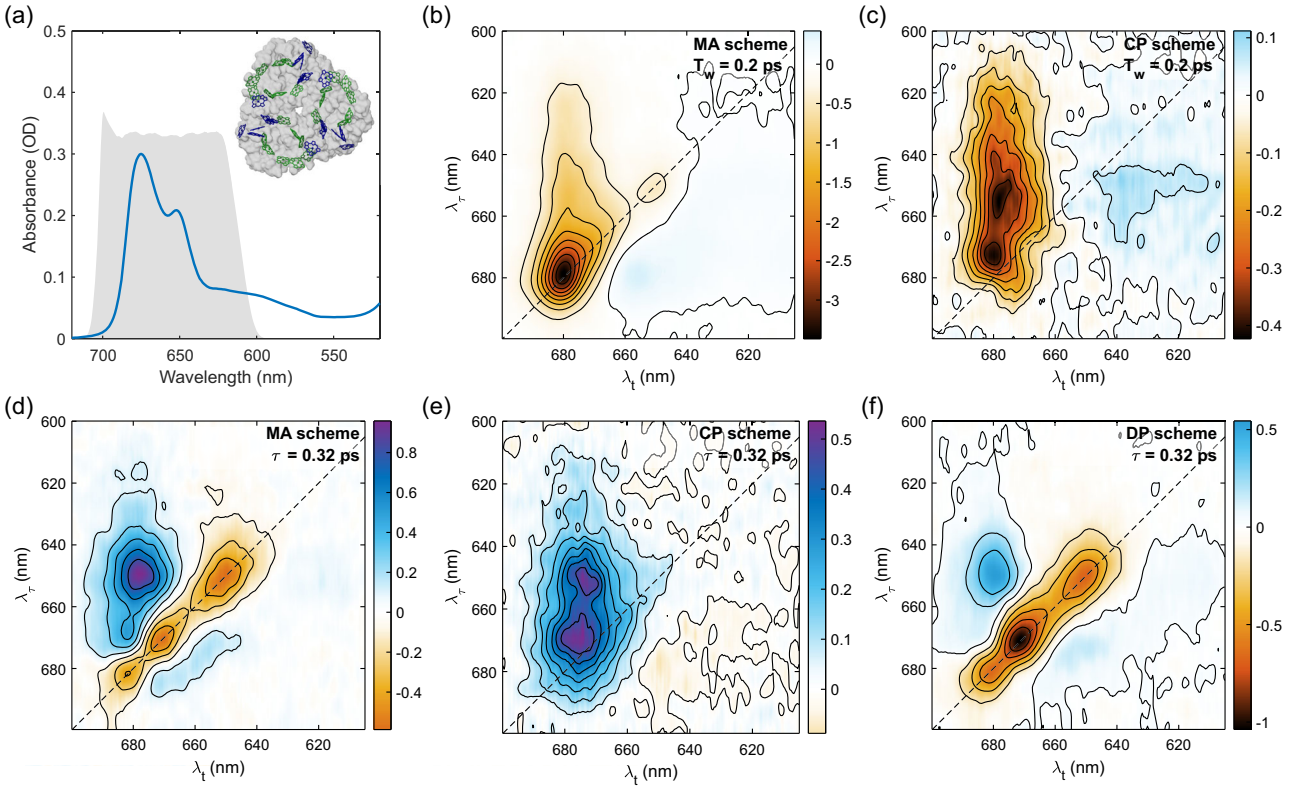

FIGURE 6 | (a) The linear absorption spectrum and protein surface structure of LHCII with embedded Chl molecules (Chl *a* in green, Chl *b* in blue). The shaded area shows the pump spectrum. (b,c) 2D spectra at $T_w = 0.2$ ps with MA and CP polarization scheme, respectively. (d–f) The first-lifetime 2D DAS of the LHCII 2D spectra with MA, CP, and DP polarization scheme, respectively.

diagonal signals in the LHCII spectra. Two discernible cross-peaks are observed at approximately 675/680 and 655/675 nm. In addition, we observe the appearances of cross-peaks on the lower-diagonal side, which reflect the uphill EET processes [51].

In Figure 6d–f, we present the first-lifetime 2D DAS (approximately at 300 fs) obtained from GLA of the LHCII 2D data under MA, CP, and DP polarization schemes. The 2D DAS derived from MA 2D spectra (Figure 6d) includes contributions from all signal pathways. It exhibits the decays of diagonal peaks near 650, 670, and 680 nm, accompanied by pronounced cross-peak growth at 650/675 nm and weaker growths connecting the 670- and 680-nm levels [52]. In the CP and DP 2D spectra, the 2D DAS (Figure 6e,f, respectively) highlight the cross-peak growth dynamics in the CP case, while decays of the diagonal peaks are more prominent in the DP results. The 2D DAS for the CP scheme (Figure 6e) shows two strong growing cross-peaks, equivalent to those observed in the MA data (Figure 6d). In addition, at 670/680 nm, the cross-peak grows with a stronger amplitude than in the MA spectra. This enhancement arises because of the absence of the diagonal decay at 670 nm, which would overlap and cancel out in the spectra using MA polarization. Along the diagonal in Figure 6e, small positive features spread across 650–680 nm. These growths of signals reflect EET processes between energetically proximate states, visible only when diagonal contributions are suppressed. Such rapid energy transfer typically occurs within strongly-coupled Chl domains (e.g. *b*601-608-609, *a*604-*b*605-606-607) [53, 54].

For the DP 2D spectra (Figure 6f), the 2D DAS mainly reflects diagonal peak dynamics, with weaker contributions from cross-peaks that involve EET between similarly oriented exciton transitions. The dominant features are the strong decays of diagonal signals, resembling the MA data but with more pronounced amplitudes, for example, at 670/670 nm. The cross-peak growths in Figure 6f appear at similar positions to those in Figure 6d for the MA spectra. Interestingly, there are instances of cross-peak growths at around 650/680 nm in both CP and DP spectra (Figure 6e,f), which could be used to determine the relative orientation between the donor and acceptor transition dipoles by comparing the DAS amplitudes, as described above. Overall, these results demonstrate that analyzing the p-2DES signals of LHCII under multiple polarization conditions provides complementary perspectives on the system's kinetics, offering new insights into its dynamic processes, spectral components, and structural organization.

4 | Discussion and Conclusion

We have demonstrated the versatility of a p-2DES implementation to obtain polarization-dependent 2D data. The implementation can be designed as a modular component to the detector arm of an existing 2D or pump-probe setup, and makes it easy to switch back to the conventional method if necessary. Inherent to the properties of 2DES, the reconstructed 2D signals retain the frequency and time resolution of the original spectra. This is especially significant in the calculation of anisotropy, whose value can be very sensitive to small errors in the spectral intensities. With this method, a 2D anisotropy map can provide a complete mapping of anisotropy kinetics between broad bandwidths

of excitation and detection wavelengths and fs time resolution, while also ensuring its reliability. This allows for anisotropic information at ultrashort timescales, in our case at $T_w = 50$ fs, much shorter than the intrinsically lower time resolution (hundreds of fs to several ps) in the pump-probe technique [55].

In this implementation, a probable source of angular error may come from the misalignment between the pump polarization and the PBC transmission axis. As mentioned in the experimental setup, these two axes must be parallel to each other in order to obtain pure polarized signals after the PBC. In the case that a small deviation occurs, that is, an angular error of $\Delta\alpha$ between these two axes, the transmitted signal in the first line of Equation (7) becomes

$$\begin{aligned}&\langle XX(\cos \text{Ø}X + \sin \text{Ø}Y)(\cos \Delta\alpha X + \sin \Delta\alpha Y)\rangle \\ &\quad = \cos \text{Ø} \cos \Delta\alpha \langle XXXX\rangle + \sin \text{Ø} \sin \Delta\alpha \langle XXYY\rangle\end{aligned} \tag{9}$$

We can see that the transmitted signal is now mixed with $\langle XXYY\rangle$. The relative strength of this contaminant scales by a factor of $\frac{\sin \text{Ø} \sin \Delta\alpha}{\cos \text{Ø} \cos \Delta\alpha} \approx \Delta\alpha \tan \text{Ø}$ (if $\Delta\alpha$ is small). Similarly, in the reflected signals, the contamination to $\langle XXYY\rangle$ is scaled with $\Delta\alpha \cot \text{Ø}$. Since we set $\text{Ø} = 45°$, the contaminants only scale with $\Delta\alpha$, indicating that the amount of unwanted signals in the transmitted and reflected parts scale directly with the misaligned angle between the pump polarization and the PBC axis. For example, a misalignment of 1° results in a signal contamination of 1.75%. Therefore, accurate alignment of the pump polarization with respect to the PBC axis should be taken carefully.

In most cases, depolarization effects due to molecular rotation observed in 2DES can be neglected at timescales shorter than 10 ps. This is because the optical transitions are often associated with relatively large molecules, whose rotational relaxation times are typically on the order of hundreds of ps or longer. For example, the rotational diffusion time measured in H_2Pc is around 400 ps (Figure 4). This contrasts with infrared spectroscopies such as 2DIR, where vibrational transitions observed in small molecules can exhibit rotational motion with timescales of few ps [16, 56, 57].

Up to this point, we only consider the incoherent signal pathways that incur a population state during T_w. There are also coherent pathways where the two pump pulses interact with different transitions, and the signal intensity during T_w exhibits oscillations corresponding to the energy gap between the states. Coherent pathways can be observed in systems where the excited states are strongly correlated by vibronic or electronic coupling, which allow the coherence between them to be strong and last long enough to be observable in experiments [10]. In principle, for oscillating signals due to vibrational coherence, as long as the Condon approximation holds, their orientational scaling factors are identical to the diagonal signals and can be suppressed in the CP polarization scheme. For electronic coherences, the scaling factors can also be derived [10], though not discussed here, and the coherences can be suppressed as long as the relative orientation between the two coupled electronic transition dipoles is known.

More polarization schemes can be implemented if their polarizations can be arbitrarily adjusted, for example, by a boxCARS geometry or using polarization pulse shaping [58]. Perhaps the most useful situation is when the two pump pulse polarizations are orthogonal to each other (one in $\hat{X}$ and one in $\hat{Y}$), and the probe pulse is polarized 45° between them. This will allow us to collect $\langle XYXY\rangle$ and $\langle XYYX\rangle$, which can be subtracted from each other and leave only signals of the coherent signal pathways, while all incoherent pathways are suppressed (diagonal or cross-peaks). This scheme is equivalent to the double-cross polarization setup [11].

In summary, the use of polarization control offers many selective enhancements and suppression to the signals appearing in 2DES spectra, allowing us to isolate and reveal spectral features and kinetics that would be obscured otherwise. We highlight an efficient implementation of the p-2DES setup, enabling polarized 2D spectra to be collected simultaneously. We have demonstrated the general use of this implementation to obtain a set of spectra with various useful polarization schemes to enhance cross-peak signals (CP), diagonal signals (DP), isotropic signal (MA), and anisotropy. We also show that suppression of any cross-peaks with known relative transition orientation is possible. The applications of the approach are demonstrated through measurements in H_2Pc and LHCII, where various spectral and dynamical information are revealed that would be hidden otherwise. The method also produces polarized signals whose amplitudes are automatically balanced, and the results offer many possibilities of reconstructing polarized 2D spectra that would otherwise take a lot more time to collect separately. This method presents a simple implementation addition to existing 2D setups, and offers more versatility to the 2DES technique.

Acknowledgments

This work was supported by grants from the Singapore Ministry of Education Academic Research Fund (Tier 1 RG92/23).

Funding

This study was supported by Ministry of Education - Singapore (Tier 1 RG92/23).

Conflicts of Interest

The authors declare no conflicts of interest.

Data Availability Statement

The data that support the findings of this study are available from the corresponding author upon reasonable request.

References

1. S. Mukamel, *Principles of Nonlinear Optical Spectroscopy* (Oxford University Press, 1995).

2. D. M. Jonas, "Two-Dimensional Femtosecond Spectroscopy," *Annual Review of Physical Chemistry* 54 (2003): 425–463.

3. F. D. Fuller and J. P. Ogilvie, "Experimental Implementations of Two-Dimensional Fourier Transform Electronic Spectroscopy," *Annual Review of Physical Chemistry* 66 (2015): 667–690.

4. E. Fresch, F. V. A. Camargo, Q. Shen, et al., "Two-Dimensional Electronic Spectroscopy," *Nature Reviews Methods Primers* 3 (2023): 84.

5. T. Brixner, J. Stenger, H. M. Vaswani, M. Cho, R. E. Blankenship, and G. R. Fleming, "Two-Dimensional Spectroscopy of Electronic Couplings in Photosynthesis," *Nature* 434 (2005): 625–628.

6. A. Gelzinis, R. Augulis, V. Butkus, B. Robert, and L. Valkunas, "Two-dimensional Spectroscopy for Non-Specialists," *Biochimica et Biophysica Acta (BBA) - Bioenergetics* 2019 (1860): 271–285.

7. S. Jana, T. N. Do, P. J. Nowakowski, et al., "Measuring the Ultrafast Correlation Dynamics of a Multilevel System Using the Center Line Slope Analysis in Two-Dimensional Electronic Spectroscopy," *The Journal of Physical Chemistry B* 127 (2023): 7309–7322.

8. H. L. Nguyen, T. N. Do, K. Zhong, et al., "Inter-Subunit Energy Transfer Processes in a Minimal Plant Photosystem II Supercomplex," *Science Advances* 10 (2024): eadh0911.

9. S. Jana, S. Prasad, H. L. Nguyen, D. V. Le, and H.-S. Tan, "Correlated Vibrational Coherence and Spectral Diffusion Analysis of Multi-Level Systems Using Two-Dimensional Electronic Spectroscopy," *The Journal of Chemical Physics* 162 (2025): 164311.

10. P. Hamm and M. Zanni, *Concepts and Methods of 2D Infrared Spectroscopy* (Cambridge University Press, 2011).

11. M. T. Zanni, N.-H. Ge, Y. S. Kim, and R. M. Hochstrasser, "Two dimensional IR Spectroscopy Can Be Designed to Eliminate the Diagonal Peaks and Expose Only the Crosspeaks Needed for Structure Determination," *Proceedings of the National Academy of Sciences* 98 (2001): 11265–11270.

12. E. Thyrhaug, R. Tempelaar, M. J. P. Alcocer, et al., "Identification and Characterization of Diverse Coherences in the Fenna-Matthews-Olson Complex," *Nature Chemistry* 10 (2018): 780–786.

13. E. Bukarté, A. Haufe, D. Paleček, C. Büchel, and D. Zigmantas, "Revealing Vibronic Coupling in Chlorophyll c1 by Polarization-Controlled 2D Electronic Spectroscopy," *Chemical Physics* 530 (2020): 110643.

14. E. L. Read, G. S. Engel, T. R. Calhoun, et al., "Cross-Peak-Specific Two-Dimensional Electronic Spectroscopy," *Proceedings of the National Academy of Sciences* 104 (2007): 14203–14208.

15. K. M. Farrell, N. Yang, and M. T. Zanni, "A Polarization Scheme that Resolves Cross-Peaks with Transient Absorption and Eliminates Diagonal Peaks in 2D Spectroscopy," *Proceedings of the National Academy of Sciences* 119 (2022): e2117398119.

16. R. M. Hochstrasser, "Two-Dimensional IR-Spectroscopy: Polarization Anisotropy Effects," *Chemical Physics* 266 (2001): 273–284.

17. R. Berera, R. van Grondelle, and J. T. M. Kennis, "Ultrafast Transient Absorption Spectroscopy: Principles and Application to Photosynthetic Systems," *Photosynthesis Research*, 101, no. 2–3, (2009): 105–118.

18. W. Xiong and M. T. Zanni, "Signal Enhancement and Background Cancellation in Collinear Two-Dimensional Spectroscopies," *Optics Letters* 33 (2008): 1371–1373.

19. J. A. Myers, K. L. Lewis, P. F. Tekavec, and J. P. Ogilvie, "Two-Color Two-Dimensional Fourier Transform Electronic Spectroscopy with a Pulseshaper," *Optics Express* 16 (2008): 17420.

20. L. P. DeFlores, R. A. Nicodemus, and A. Tokmakoff, "Two-Dimensional Fourier Transform Spectroscopy in the Pump-Probe Geometry," *Optics Letters* 32 (2007): 2966–2968.

21. D. V. Voronine, D. Abramavicius, and S. Mukamel, "Manipulating Multidimensional Electronic Spectra of Excitons by Polarization Pulse Shaping," *The Journal of Chemical Physics* 126 (2007): 044508.

22. J. Dreyer, A. M. Moran, and S. Mukamel, "Tensor Components in Three Pulse Vibrational Echoes of a Rigid Dipeptide," *Bulletin of the Korean Chemical Society* 24 (2003): 1091–1096.

23. J. Wang, R. Zhu, J. Zou, et al., "Incoherent Ultrafast Energy Transfer in phycocyanin 620 from Thermosynechococcus Vulcanus Revealed by Polarization-Controlled Two Dimensional Electronic Spectroscopy," *The Journal of Chemical Physics* 161 (2024): 085101.

24. Y. Song, A. Schubert, E. Maret, et al., "Vibronic Structure of Photosynthetic Pigments Probed by Polarized Two-Dimensional Electronic Spectroscopy and Ab Initio Calculations," *Chemical Science* 10 (2019): 8143–8153.

25. S. C. Massey, P.-C. Ting, S.-H. Yeh, et al., "Orientational Dynamics of Transition Dipoles and Exciton Relaxation in LH2 from Ultrafast Two-Dimensional Anisotropy," *The Journal of Physical Chemistry Letters* 10 (2019): 270–277.

26. G. S. Schlau-Cohen, T. R. Calhoun, N. S. Ginsberg, M. Ballottari, R. Bassi, and G. R. Fleming, "Spectroscopic Elucidation of Uncoupled Transition Energies in the Major Photosynthetic Light-Harvesting Complex, LHCII," *Proceedings of the National Academy of Sciences* 107 (2010): 13276–13281.

27. E. L. Read, G. S. Schlau-Cohen, G. S. Engel, J. Wen, R. E. Blankenship, and G. R. Fleming, "Visualization of Excitonic Structure in the Fenna-Matthews-Olson Photosynthetic Complex by Polarization-Dependent Two- Dimensional Electronic Spectroscopy," *Biophysical Journal* 95 (2008): 847–856.

28. X. Leng, Y. Yan, R. Zhu, J. Zou, W. Zhang, and Q. Shi, "Revealing Intermolecular Electronic and Vibronic Coherence with Polarization-Dependent Two-Dimensional Beating Maps," *The Journal of Physical Chemistry Letters* 14 (2023): 838–845.

29. R. D. Mehlenbacher, J. Wang, N. M. Kearns, et al., "Ultrafast Exciton Hopping Observed in Bare Semiconducting Carbon Nanotube Thin Films with Two-Dimensional White-Light Spectroscopy," *The Journal of Physical Chemistry Letters* 7 (2016): 2024–2031.

30. F. Perakis and P. Hamm, "Two-Dimensional Infrared Spectroscopy of Neat Ice Ih," *Physical Chemistry Chemical Physics* 14 (2012): 6250–6256.

31. M. Ji, M. Odelius, and K. J. Gaffney, "Large Angular Jump Mechanism Observed for Hydrogen Bond Exchange in Aqueous Perchlorate Solution," *Science* 328 (2010): 1003–1005.

32. S. Woutersen and P. Hamm, "Structure Determination of Trialanine in Water Using Polarization Sensitive Two-Dimensional Vibrational Spectroscopy," *The Journal of Physical Chemistry B* 104 (2000): 11316–11320.

33. N. S. Ginsberg, J. A. Davis, M. Ballottari, Y.-C. Cheng, R. Bassi, and G. R. Fleming, "Solving Structure in the CP29 Light Harvesting Complex with Polarization-Phased 2D Electronic Spectroscopy," *Proceedings of the National Academy of Sciences* 108 (2011): 3848–3853.

34. E. Thyrhaug, K. Žídek, J. Dostál, D. Bína, and D. Zigmantas, "Exciton Structure and Energy Transfer in the Fenna-Matthews-Olson Complex," *The Journal of Physical Chemistry Letters* 7 (2016): 1653–1660.

35. Y. Song, A. Konar, R. Sechrist, et al., "Multispectral Multidimensional Spectrometer Spanning the Ultraviolet to the Mid-Infrared," *The Review of Scientific Instruments* 90 (2019): 013108.

36. Y. Xu, L. Mewes, E. Thyrhaug, et al., "Isolating Pure Donor and Acceptor Signals by Polarization- Controlled Transient Absorption Spectroscopy," *The Journal of Physical Chemistry Letters* 14 (2023): 5390–5396.

37. T. Ha, T. A. Laurence, D. S. Chemla, and S. Weiss, "Polarization Spectroscopy of Single Fluorescent Molecules," *The Journal of Physical Chemistry B* 103 (1999): 6839–6850.

38. P. M. Donaldson, R. F. Howe, A. P. Hawkins, M. Towrie, and G. M. Greetham, "Ultrafast 2D-IR Spectroscopy of Intensely Optically Scattering Pelleted Solid Catalysts," *The Journal of Chemical Physics* 158 (2023): 114201.

39. H.-S. Tan, I. R. Piletic, and M. D. Fayer, "Polarization Selective Spectroscopy Experiments: Methodology and Pitfalls," *Journal of the Optical Society of America B* 22 (2005): 2009–2017.

40. H. Van Mingroot, S. De Backer, J. van Stam, M. Van der Auweraer, and F. C. De Schryver, "The Emission at 669 nm of Metal Free Phthalocyanine in Toluene and 1-Bromonaphthalene Solutions," *Chemical Physics Letters* 253 (1996): 397–402.

41. D. M. Jonas, M. J. Lang, Y. Nagasawa, T. Joo, and G. R. Fleming, "Pump- Probe Polarization Anisotropy Study of Femtosecond Energy Transfer Within the Photosynthetic Reaction Center of Rhodobacter Sphaeroides R26," *The Journal of Physical Chemistry* 100 (1996): 12660–12673.

42. Y. J. Shiu, Y. Shi, M. Hayashi, C. Su, K. L. Han, and S. H. Lin, "Femtosecond Spectroscopy Study of Electronically Excited States of Chlorophyll a Molecules in Ethanol," *Chemical Physics Letters* 378 (2003): 202–210.

43. I. H. M. van Stokkum, D. S. Larsen, and R. van Grondelle, "Global and Target Analysis of Time-Resolved Spectra," *Biochimica et Biophysica Acta (BBA) - Bioenergetics* 2004 (1657): 82–104.

44. K. Kwak, S. Park, I. J. Finkelstein, and M. D. Fayer, "Frequency-Frequency Correlation Functions and Apodization in Two-Dimensional Infrared Vibrational Echo Spectroscopy: A New Approach," *The Journal of Chemical Physics* 127 (2007): 124503.

45. S. T. Roberts, J. J. Loparo, and A. Tokmakoff, "Characterization of Spectral Diffusion from Two-Dimensional Line Shapes," *The Journal of Chemical Physics* 125 (2006): 084502.

46. R. Blankenship, *Molecular Mechanisms of Photosynthesis* (Wiley, 2014).

47. H. van Amerongen and R. Croce, "Non-Photochemical Quenching in Plants: Mechanisms and Mysteries," *The Plant Cell* 37 (2025): koaf240.

48. G. S. Schlau-Cohen, T. R. Calhoun, N. S. Ginsberg, et al., "Pathways of Energy Flow in LHCII from Two-Dimensional Electronic Spectroscopy," *The Journal of Physical Chemistry B* 113 (2009): 15352–15363.

49. S. Caffarri, R. Kouřil, S. Kereïche, E. J. Boekema, and R. Croce, "Functional Architecture of Higher Plant Photosystem II Supercomplexes," *The Embo Journal* 28 (2009): 3052–3063.

50. E. Betti, P. Saraceno, E. Cignoni, L. Cupellini, and B. Mennucci, "Insights into Energy Transfer in Light-Harvesting Complex II Through Machine-Learning Assisted Simulations," *The Journal of Physical Chemistry B* 128 (2024): 5188–5200.

51. P. Akhtar, C. Zhang, Z. Liu, H.-S. Tan, and P. H. Lambrev, "Excitation Transfer and Trapping Kinetics in Plant Photosystem I Probed by Two-Dimensional Electronic Spectroscopy," *Photosynthesis Research* 135 (2018): 239–250.

52. P. Akhtar, T. N. Do, P. J. Nowakowski, et al., "Temperature Dependence of the Energy Transfer in LHCII Studied by Two-Dimensional Electronic Spectroscopy," *The Journal of Physical Chemistry B* 123 (2019): 6765–6775.

53. T. Renger, M. E. Madjet, A. Knorr, and F. Müh, "How the Molecular Structure Determines the Flow of Excitation Energy in Plant Light-Harvesting Complex II," *Journal of Plant Physiology* 168 (2011): 21330003.

54. V. Novoderezhkin, A. Marin, and R. van Grondelle, "Intra- and Inter-Monomeric Transfers in the Light Harvesting LHCII Complex: The Redfield-Forster Picture," *Physical Chemistry Chemical Physics* 13 (2011): 21866281.

55. H. L. Nguyen, K. Zhong, T. N. Do, et al., "Directly Measuring the Connectivity Between Isoenergetic Light-Harvesting Antennas in Plant Photosystem II at Physiological Temperature," *The Journal of Physical Chemistry Letters* 17 (2025): 605–614.

56. R. M. Hochstrasser, "Studies of Fast Inertial and Diffusive Motions in Liquids," *Hyperfine Interactions* 38 (1987): 633–650.

57. H.-S. Tan, I. R. Piletic, and M. D. Fayer, "Orientational Dynamics of Water Confined on a Nanometer Length Scale in Reverse Micelles," *The Journal of Chemical Physics* 122 (2005): 174501.

58. C. T. Middleton, D. B. Strasfeld, and M. T. Zanni, "Polarization Shaping in the Mid-IR and Polarization-Based Balanced Heterodyne Detection with Application to 2D IR Spectroscopy," *Optics Express* 17 (2009): 14526–14533.

Appendix

Automatic Balancing Between the Parallel and Perpendicular Signals

The collected polarized signals in our p-2DES setup are automatically balanced. The essential component in $\langle XXXX \rangle$ and $\langle XXYY \rangle$ are the response functions $R_{\parallel}$ and $R_{\perp}$, respectively. If we can measure both $R_{\parallel}$ and $R_{\perp}$ similarly (up to a same proportional constant), then the measurement is deemed balanced. Let us first consider the signal dataset which measures $\langle XXXX \rangle$. The resulting signal field $E_{s_{\parallel}}$ scales as

$$E_{s_{\parallel}} = k_{\parallel} E_p^* E_p E_{pr} R_{\parallel} \tag{A.1}$$

where E_p and E_{pr} are the pump and probe electric field amplitudes interacting with the sample. The $k_{\parallel}$ factor accounts for the reduction of $\cos \emptyset$ in Equation (7) when we project the probe beam to the parallel component, and also the efficiency of the subsequent optical elements throughput, including the PBC, reflective optics, spectrometer diffraction grating and CCD detector. The probe beam which travels collinearly with the signal is, likewise, scaled by the same factor

$$E_{pr_{\parallel}} = k_{\parallel} E_{pr} \tag{A.2}$$

In general, the factors $k_{\parallel}$, and analogously $k_{\perp}$ for the $\langle XXYY \rangle$ measurement, are different, as the perpendicular component of the probe beam may not be the same amplitude as the parallel (i.e. $\emptyset \neq 45°$), and will also traverse through different optics after the PBC. On the surface, it may seem that the measured $\langle XXXX \rangle$ and $\langle XXYY \rangle$ will therefore not be balanced, and hence some kind of normalization or referencing will be needed. It will be shown here that in fact, the measurement and data processing procedure will eliminate the $k_{\parallel}$ and $k_{\perp}$ factors.

Considering the $\langle XXXX \rangle$ channel again, the signal and probe fields at detection follow the square law

$$S_{on_{\parallel}} = |E_{pr_{\parallel}} + E_{s_{\parallel}}|^2 \tag{A.3}$$

$$\approx |E_{pr_{\parallel}}|^2 + 2Re\left(E_{pr_{\parallel}}^* E_{s_{\parallel}}\right) \tag{A.4}$$

where the term $|E_{s_{\parallel}}|^2$ is dropped as it is usually much smaller than the other two terms. The "on" denotes "pump on". We also detect the probe field with "pump off", that is, without signal

$$S_{off_{\parallel}} = |E_{pr_{\parallel}}|^2 \tag{A.5}$$

The collected spectra are then processed by taking

$$\log \frac{S_{on_{\parallel}}}{S_{off_{\parallel}}} = \log \frac{|E_{pr_{\parallel}}|^2 + 2Re\left(E_{pr_{\parallel}}^* E_{s_{\parallel}}\right)}{|E_{pr_{\parallel}}|^2} \tag{A.6}$$

$$= \log \left[1 + \frac{2Re\left(E_{pr_{\parallel}}^* E_{s_{\parallel}}\right)}{|E_{pr_{\parallel}}|^2}\right] \tag{A.7}$$

$$= \log \left[1 + \frac{2k_{\parallel}^2 Re\left(E_{pr}^* E_p^* E_p E_{pr} R_{\parallel}\right)}{k_{\parallel}^2 |E_{pr}|^2}\right] \tag{A.8}$$

$$= \log\left[1 + 2Re\left(E_p^* E_p R_\parallel\right)\right] \tag{A.9}$$

$$\approx \frac{2Re\left(E_p^* E_p R_\parallel\right)}{\ln 10} \tag{A.10}$$

Crucially, the measured $\langle XXXX \rangle = \log \frac{S_{on_\parallel}}{S_{off_\parallel}}$ signal is independent of the factor $k_\parallel$. The same argument applies to the $\langle XXYY \rangle$ channel where the processed signal $\frac{2Re\left(E_p^* E_p R_\perp\right)}{\ln 10}$ is obtained, likewise without the $k_\perp$ factor. With $R_\parallel$ and $R_\perp$ collected with the same multiplying constant, and hence balanced, they can be linearly combined directly to yield the desired polarization schemes.